



## Theoretical prediction by DFT on properties of $\beta'$ -SrTa<sub>2</sub>O<sub>6</sub> crystal

Murat Aycibin<sup>1,2,\*</sup>, Mehmet Erzen<sup>3</sup>, Harun Akkus<sup>1</sup>

<sup>1</sup>Department of Physics, Faculty of Science, Van Yuzuncu Yil University, 65080, Van, Turkey

<sup>2</sup>Vocational School of Technical Sciences, Department of Medical Services and Techniques, Mersin University, 33334 Mersin, Turkey

<sup>3</sup>Department of Physics, Institute of Natural and Applied Sciences, Van Yuzuncu Yil University, 65080, Van, Turkey

Received 16 May 2022; Received in revised form 18 August 2022; Accepted 14 November 2022

### Abstract

Based on the Density Functional Theory (DFT) electronic band structure, state density, linear optics, elastic, dynamic and thermodynamic properties of  $\beta'$ -SrTa<sub>2</sub>O<sub>6</sub> crystal with P4/mbm (No. 127) space group were investigated with the help of ABINIT and Wien2k code. In the study, it was found that the  $\beta'$ -SrTa<sub>2</sub>O<sub>6</sub> crystal is classified as a semiconductor with an indirect bandgap. For this crystal, the dielectric function was obtained and optical constants such as energy loss function, extinction coefficient, absorption coefficient and reflectivity were calculated. The components of the elastic stiffness tensor, the phonon dispersion, the state density and the contribution of each atom to the state density were obtained. Finally, thermodynamic properties were determined for the  $\beta'$ -SrTa<sub>2</sub>O<sub>6</sub> crystal. Furthermore, the changes in free energy ( $F$ ), internal energy ( $E$ ), entropy ( $S$ ) and heat capacity ( $C$ ) depending on the temperature were investigated.

**Keywords:** DFT, electronic structure, elastic/optical/thermodynamic properties,  $\beta'$ -SrTa<sub>2</sub>O<sub>6</sub> crystal

### I. Introduction

Due to a wide range of compositions and their desirable properties, such as microwave dielectric properties [1,2], superconductivity [3], antiferromagnetism [4], semiconductor behaviour with a narrow band gap [5], catalytic selectivity [6,7], ferromagnetic behaviour [8], being suitable host for laser applications [7,9] and superior electrochemical performances [10], AB<sub>2</sub>O<sub>6</sub> compounds (A and B include main group and transition metal cations), have been interesting materials to investigate.

One of the compounds belonging to the AB<sub>2</sub>O<sub>6</sub> family is SrTa<sub>2</sub>O<sub>6</sub> (STO) related to orthorhombic CaTa<sub>2</sub>O<sub>6</sub>. In the literature, there are many experimental works devoted to STO and its derivatives. Bayer and Gruehn [11] synthesized and investigated STO compound. They revealed the compound's lattice parameters and observed that orthorhombic STO transforms to tetragonal tungsten bronze (TTB) structure STO at a temperature value above 1220 °C in air. Kunin *et al.* [12] prepared thin

film strontium tantalite to investigate its temperature and frequency dependence of electrical conductivity,  $\epsilon$  and  $\tan \delta$ . Bi<sub>2</sub>O<sub>3</sub> and STO form strontium bismuth tantalate used by Lee and Jung to fabricate Pt/SrBi<sub>2</sub>Ta<sub>2</sub>O<sub>9</sub>/Pt capacitors [13]. Ollivier and Mallouk [14] used a chimie douce reaction to obtain STO. In addition, STO was also synthesized by a solid-state reaction and its band gap value was measured [15]. Tokimitsu *et al.* [16] used SrTa<sub>2</sub>O<sub>6</sub>/SiON stacked-layer as an "I" layer in MFMIS structures. They emphasized that the physical properties of STO have not been well known. The plasma-enhanced atomic layer deposition method was used to prepare STO thin films to investigate their electrical properties with increasing annealing temperatures [17]. Sakamoto *et al.* [18] used the chemical solution deposition method to fabricate (Sr,Ba)(Nb,Ta)<sub>2</sub>O<sub>6</sub> thin films. The electrical characterization of the STO thin films was reported by Chae *et al.* [19]. Regnery *et al.* [20] grew STO thin films for high- $k$  dielectric application purposes via chemical vapour deposition on various substrates. STO thin films with different thicknesses were deposited in a multi-wafer planetary MOCVD reactor combined with a TRIJET liquid delivery system to investigate their electrical properties for MIM and MIS

\*Corresponding author: tel: +90 531 2775651

e-mail: aycibin@gmail.com, murataycibin@mersin.edu.tr

applications [21]. Silinskas *et al.* [22] prepared STO thin films using the metalorganic chemical vapour deposition method to investigate the annealing temperature effects on electrical properties. Muthurajan *et al.* [23] used the hydroxide precursor method to synthesize STO at low temperatures. Lu *et al.* [24] investigated thickness dependence of interface between STO thin films and Pt electrodes and defects in STO thin films. The crystal structures of two out of three phases of STO were studied by Kim *et al.* [25]. Lu and co-workers [26] investigated the capacitance-voltage and leakage-current characteristics of amorphous and crystalline STO thin films. Lu *et al.* [27] doped STO thin films with Si and Ti impurities to monitor their effects on the electrical properties of sol-gel derived amorphous STO thin films. STO was doped with  $\text{Pr}^{3+}$  ion to prepare red-emitting phosphor [28]. STO was used to fabricate the  $\text{Ag-SrTa}_2\text{O}_6/\text{g-C}_3\text{N}_4$  photocatalyst system [29]. The dielectric properties of  $\beta$  and  $\beta'$ - $\text{SrTa}_2\text{O}_6$  crystal structures were measured using phase pure ceramic specimens [30]. A semiconductor heterojunction  $\text{SrTa}_2\text{O}_6/\text{g-C}_3\text{N}_4$  was fabricated to measure its visible-light photocatalytic properties [31]. STO thin films were used for gate insulators to improve InGaZnO thin films [32,33].

After a comprehensive search through the literature, we could not find any theoretical work which was devoted to understanding the properties of STO compound. In this work, the electronic, structural, optical, dynamic and thermodynamic properties of STO compound were investigated via theoretical approach. This study may be a guide for researchers who will do more research on STO or compounds including STO to reveal the potential use of the compound in the technological area.

## II. Details of calculation

The experimental parameters, which were used as initial parameters to construct structural file for Wien2k [34] and ABINIT [35] computational codes, were reported by Kim *et al.* [25,30]. The unit cell of STO was drawn by the Vesta 3 [36] and is given in Fig. 1. Wien2k was used as a tool to calculate electronic, structural and optical properties of STO via Density Functional Theory (DFT), which plays important role in understanding structure-property relations. In the calculation, the

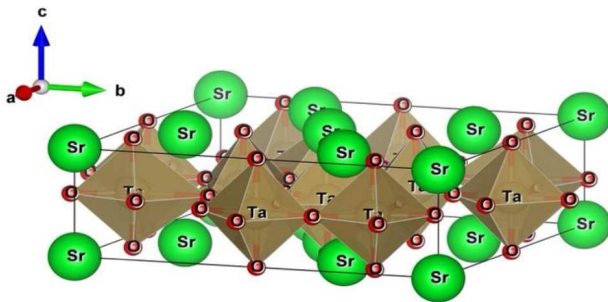


Figure 1. The unit cell of  $\beta'$ - $\text{SrTa}_2\text{O}_6$  crystal

exchange-correlation energy is treated within the GGA as parametrized by Perdew *et al.* [37] and suggested by Wien2k. However, it is a well-known fact that DFT underestimates the bandgap value of material compared to experimentally determined [38]. Therefore, Tran-Blaha modified Becke-Jonhson (TB-mBJ) potential [39] was used to predict the energy band gap of any compound more accurately. Moreover, the threshold energy between valence and core states is taken to be  $-8.0$  Ry.

The elastic, dynamic and thermodynamic properties were calculated within the ABINIT package program. In ABINIT calculation, the Trouillier-Martins type [40] self-consistent norm-conserving pseudopotentials generated by FHI (FHI98PP) code [41] were used in all calculations. In addition, while making these calculations, valence electrons  $5s^2$  for strontium (Sr),  $5d^3$  and  $6s^2$  for tantalum (Ta) and  $2s^2$  and  $2p^4$  for oxygen (O) were considered. The total valence electrons are 12 for Sr, 50 for Ta, and 180 for O. Therefore, the compound  $\beta'$ - $\text{SrTa}_2\text{O}_6$  has 121 valence electrons. All calculations with ABINIT were based on local density approximation (LDA) for the solution of Kohn-Sham equations [42] and  $20$  Hartree and  $2 \times 2 \times 2$  Monkhorst-Pack mesh grids were selected for cut-off energy and Brillouin zone (BZ), respectively.

## III. Results and discussion

### 3.1. Structural optimization

Structural optimization was made for the base case with the Wien2k package program, using the lattice parameters and atomic positions given by Lee *et al.* [43]. The volume optimization process in Wien2k was used to obtain the theoretical lattice parameters, which are within 1% of those obtained experimentally (Fig. 2). The optimized lattice parameters were used in the rest of the calculations.

### 3.2. Electronic band structure

To evaluate a compound whether it could be used in technological areas, it is important to reveal its physical properties. Figure 3 demonstrates the electronic

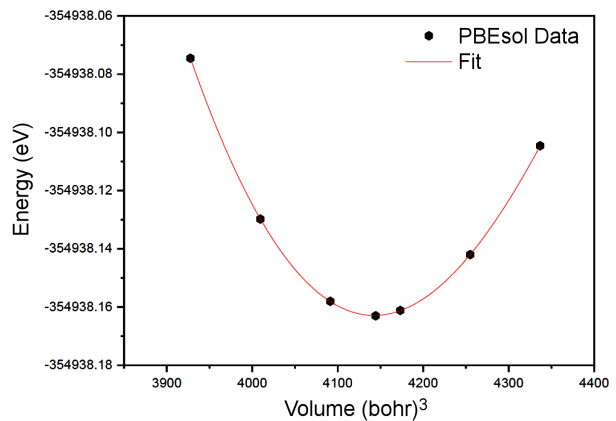


Figure 2. Volume optimization of  $\beta'$ - $\text{SrTa}_2\text{O}_6$  crystal

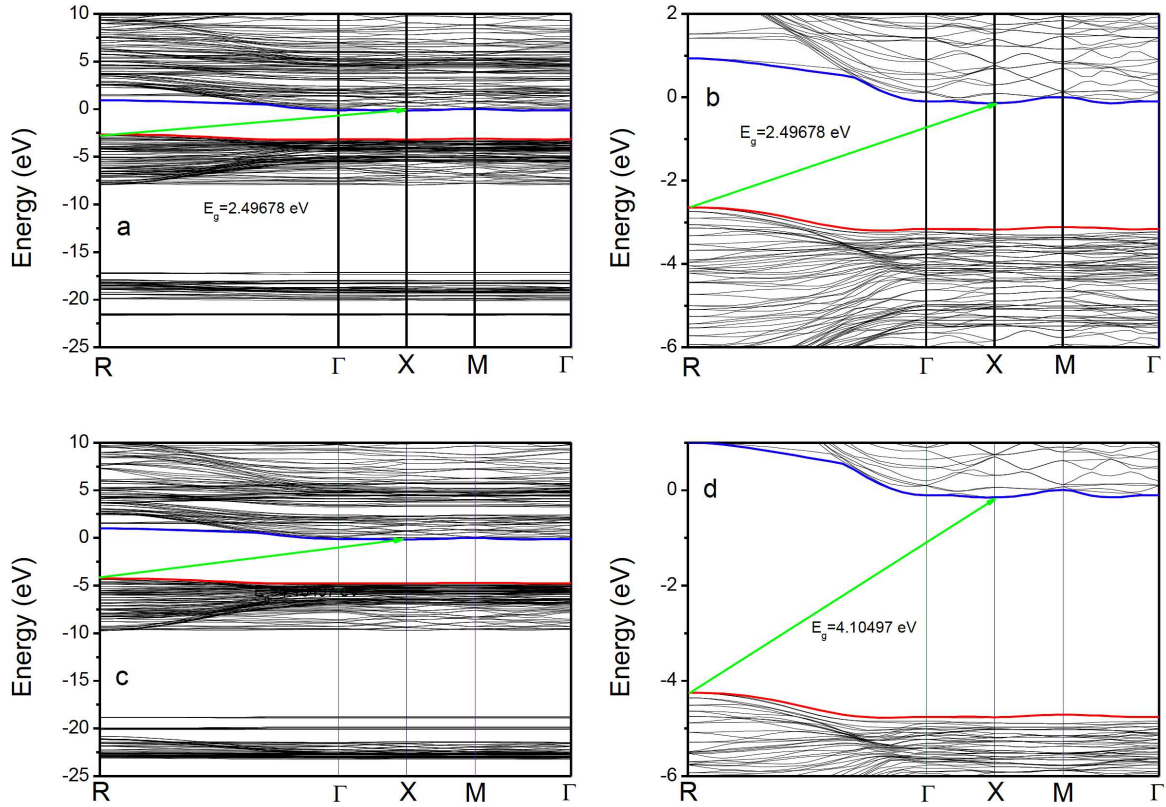


Figure 3. Electronic band structure of  $\beta'$ -SrTa<sub>2</sub>O<sub>6</sub> crystal a-b) PBEsol-GGA; c-d)TB-mBJ

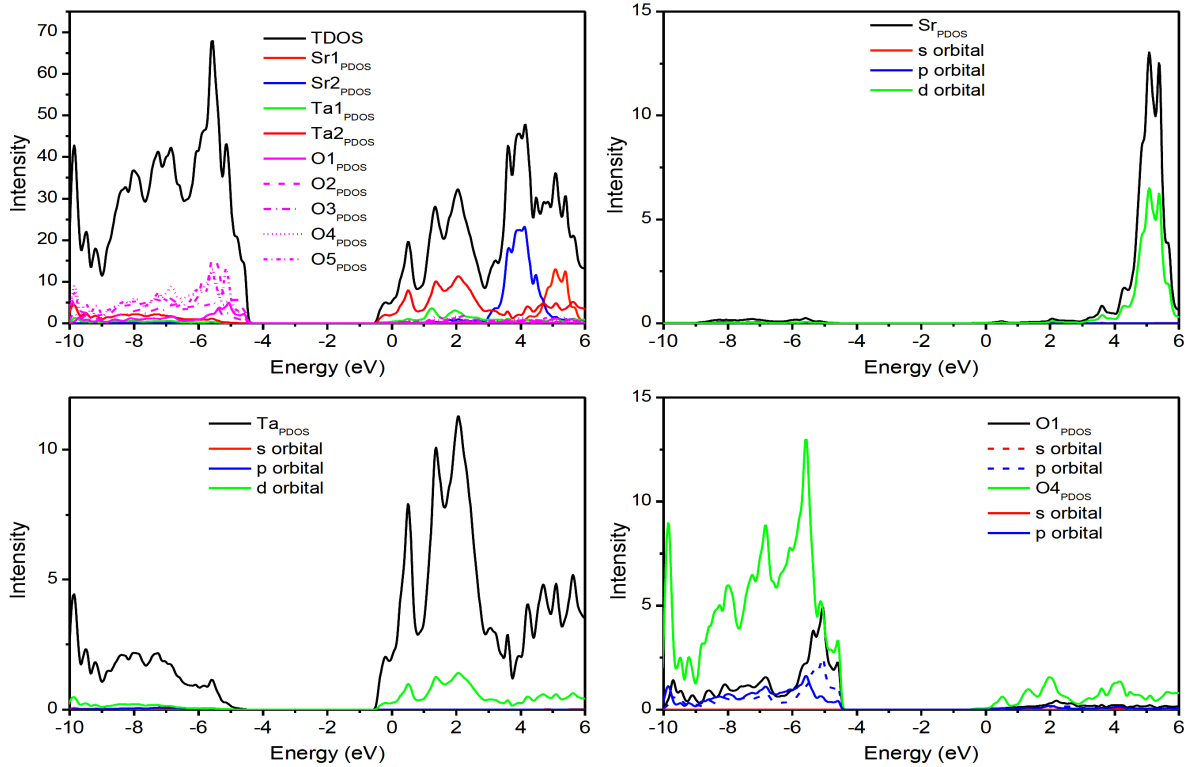
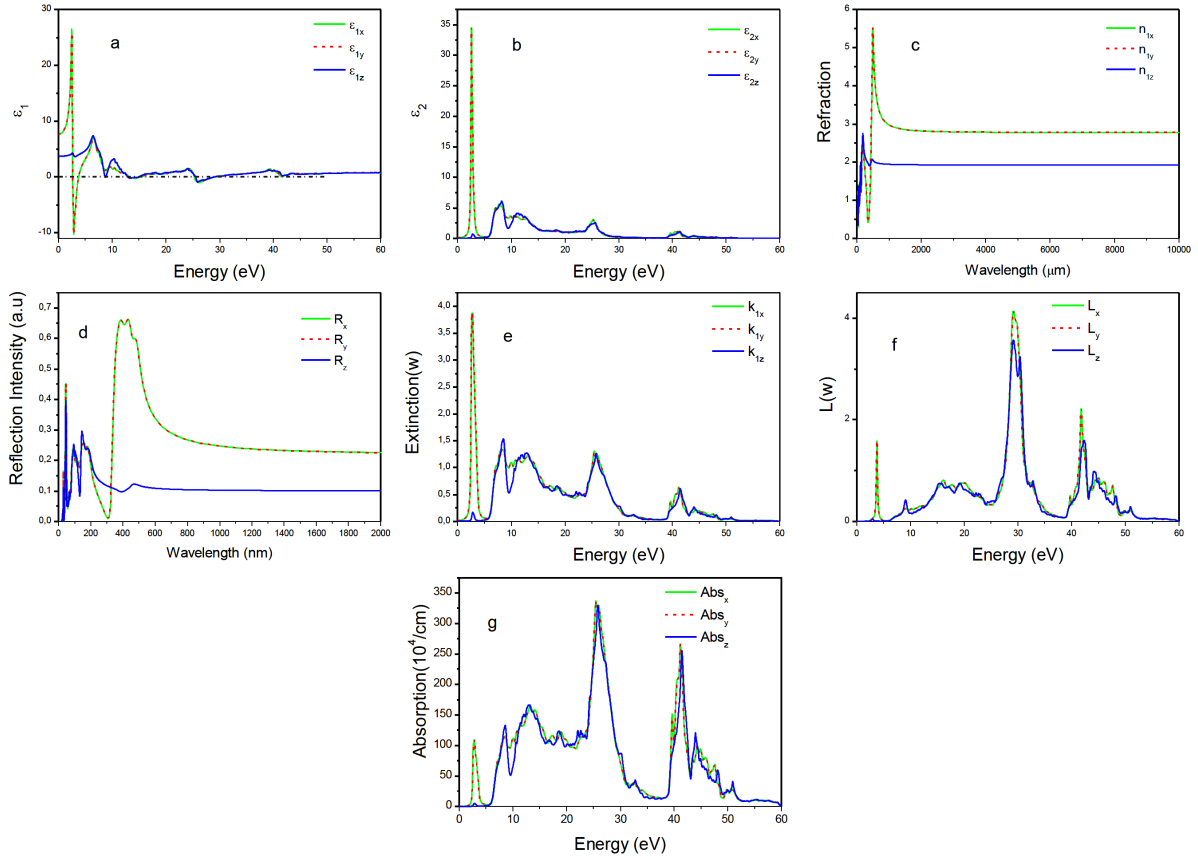


Figure 4. Total (TDOS) and partial density of states (PDOS) of  $\beta'$ -SrTa<sub>2</sub>O<sub>6</sub> crystal

band structure of  $\beta'$ -SrTa<sub>2</sub>O<sub>6</sub> crystal along with different high symmetry  $k$ -directions at equilibrium volume with the PBEsol-GGA (Fig. 3a,b) and TB-mBJ (Fig. 3c,d) schemes. The indirect fundamental bandgap behaviour

appears between the topmost valence band at the R point and at the bottom of the conduction band at  $\Gamma$  point. The calculated indirect band gap values are 2.45 and 4.10 eV for PBEsol-GGA and PBEsol-GGA+TB-mBJ poten-



**Figure 5.** Real (a) and imaginary (b) components of the dielectric function and optical constants (c-g) in different crystal axis for  $\beta'$ -SrTa<sub>2</sub>O<sub>6</sub> crystal

tials, respectively. Note that the GGA method usually underestimates the value of the energy bandgap energy [44]. Moreover, it is seen that TB-mBJ (Fig. 3c,d) predicts the energy bandgap value of the compound more accurately which is in a good agreement with the experimentally obtained value [15]. A wide bandgap makes the compound a good candidate for optoelectronic applications, therefore, the examined compound is a good candidate due to the wide gap band gap value of around 4.1 eV.

The total and partial density of states of the compound are calculated and shown in Fig. 4. The O-2*p* states are mainly predominant in the valence band. It is seen that there is hybridization between Sr-3*d* and Ta-4*d* states in the conduction band.

### 3.3. Optical properties

Semiconductors have a very important place in the field of science and technology. They have wide application potential in different fields such as semiconductor lasers and detectors. The optical properties of solids, which have been used to determine where compounds could be used, are very important for fundamental research and industrial applications. When light interacts with matter, light is either absorbed, reflected or passed through. These three processes constitute the response of matter to the incoming electromagnetic wave and can be characterized by the frequency-dependent complex

dielectric function. These real and imaginary parts are linked by Kramers-Kronig relations.

In this study, the optical properties of  $\beta'$ -SrTa<sub>2</sub>O<sub>6</sub> crystal were investigated. The real and imaginary parts of the dielectric function for this crystal structure are given in Figs. 5a,b, respectively, for different crystal axes. The first analysis reveals anisotropy of light interaction immediately in Fig. 5.

Careful analysis reveals that the real part of the dielectric function, which is related to the polarization of the medium, descends into the negative region in all crystal axis directions. This character implies the presence of reflection. In other words, in these regions, the compound optically shows metallic properties. The values of the static dielectric constant of the  $\beta'$ -SrTa<sub>2</sub>O<sub>6</sub> crystal in the direction of different crystal axes were calculated as  $\epsilon_{1x} = \epsilon_{1y} = 7.67$ , and  $\epsilon_{1z} = 3.7$ .

The variation of the refractive index versus the wavelength in different crystal axes of the  $\beta'$ -SrTa<sub>2</sub>O<sub>6</sub> crystal was examined and obtained (Fig. 5c). The values of the refractive index in the direction of different crystal axes were calculated as  $n_{1x} = n_{1y} = 2.78$ , and  $n_{1z} = 1.93$ , respectively.

The extinction coefficient (Fig. 5e) had a similar character as the imaginary part of the dielectric constant as it starts to increase from the threshold which was represented by the optical bandgap.

Reflectivity and energy loss function are calculated

**Table 1. Computed elastic stiffness tensors for  $\beta'$ -SrTa<sub>2</sub>O<sub>6</sub> crystal (GPa)**

$C_{ij}$	1	2	3	4	5	6
1	530.60593	210.34418	90.46035	0	0	0
2	210.88445	529.78587	90.39248	0	0	0
3	90.18706	91.04782	497.62943	0	0	0
4	0	0	0	69.50015	0	0
5	0	0	0	0	67.84603	0
6	0	0	0	0	0	164.82122

**Table 2. Computed elastic compliance tensors for  $\beta'$ -SrTa<sub>2</sub>O<sub>6</sub> crystal (1/GPa)**

$S_{ij}$	1	2	3	4	5	6
1	0.00227	-0.00086	-0.00026	$2.89804 \cdot 10^{-11}$	$-1.19483 \cdot 10^{-9}$	$9.81639 \cdot 10^{-8}$
2	-0.00086	0.00227	-0.00026	$2.90216 \cdot 10^{-11}$	$-1.19699 \cdot 10^{-9}$	$9.82939 \cdot 10^{-8}$
3	-0.00025	-0.00026	0.00210	$7.45059 \cdot 10^{-11}$	$-5.22868 \cdot 10^{-9}$	$2.07081 \cdot 10^{-7}$
4	0	0	0	0.01439	0	0
5	0	0	0	0	0.01474	0
6	0	0	0	0	0	0.00607

and illustrated in Figs. 5d and 5f, respectively. The analysis of reflective spectra reveals that 80% of the incoming light is reflected and 20% goes through the UV region and almost all light is reflected at 300 nm. Then it starts to increase and reaches a peak where 70% of the light goes through the material in the zone corresponding to the visible region. Then, the reflectivity decreases rapidly to around 30% of incoming light for higher wavelength values.

The energy loss function,  $L(w)$ , describes the energy loss of a fast electron penetrating through the material. Analysis of  $L(w)$  shows that four peaks appear in the spectrum and they represent a property associated with plasmon resonance. The important peak of the  $L(w)$  function is located at energy 30 eV.

The linear absorption spectrum is given in Fig. 5g. The energy gap corresponding to the absorption threshold starts at 4.1 eV. The absorption threshold is due to the electronic transition from the valence band to the conduction band.

### 3.4. Elastic, dynamic and thermodynamic properties

To determine the mechanical stability of the  $\beta'$ -SrTa<sub>2</sub>O<sub>6</sub> crystal, the components of the elastic stiffness tensor ( $C_{ij}$ ) and the corresponding elastic compliance tensor ( $S_{ij}$ ) were calculated and listed in Tables 1 and 2. To satisfy mechanical stability criteria for the tetragonal system, the components of the elastic tensor satisfy the following requirements [45]:

$$C_{ii} > 0, \quad i = 1, 3, 4, 6 \quad (1)$$

$$C_{11} > C_{12} \quad (2)$$

$$C_{11} + C_{22} - C_{12} > 0 \quad (3)$$

$$2C_{11} + C_{22} + C_{12} > 0 \quad (4)$$

It is easily seen from Table 1 that all calculated elastic constants obey the generalized stability criteria of tetragonal crystal requirements. Therefore, the compound of interest is mechanically stable. Moreover, the

elastic constant reflects the directional resistance under the stress. For example,  $C_{11}$  and  $C_{33}$  indicate the resistance to linear compression along the  $a$ -axis and  $c$ -axis, respectively. The values of  $C_{11}$  and  $C_{33}$  are very large (Table 1) which implies that the compound is incompressible under uniaxial stress along the  $x$  and  $z$  axes. Furthermore,  $C_{11} > C_{33}$  means that the  $z$ -axis is more compressible than the  $x$ -axis.

The polycrystalline elastic properties such as bulk modulus, shear modulus, Young modulus etc. were calculated through the Voigt-Reuss-Hill method [46] and inserted in Table 3. In addition to the above parameters, Poisson ratio, flexibility coefficient, Debye temperature, etc. were listed in Table 3. It is a well-known fact that material with a higher bulk modulus value is more incompressible. Shear modulus indicates the resistance of material to the shape changes under shear stress. The ratio of stress to strain is represented by Young modulus,  $E$ , which is regarded as a standard of solid stiffness. All three parameters mentioned above are inserted in Table 3.

**Table 3. Computed elastic property for  $\beta'$ -SrTa<sub>2</sub>O<sub>6</sub> crystal**

Property	Value
Voigt Bulk modulus, $B_V$ [GPa]	260.046
Reuss Bulk modulus, $B_R$ [GPa]	256.102
Bulk modulus VRH average, $B_{VRH}$ [GPa]	258.074
Voigt Shear modulus, $G_V$ [GPa]	138.222
Reuss Shear modulus, $G_R$ [GPa]	108.977
Shear modulus VRH average, $G_{VRH}$ [GPa]	123.599
Young modulus, $E$ [GPa]	319.752
Poisson ratio, $\nu$ [-]	0.294
Flexibility coefficient, $K$ [-]	2.088
Debye temperature, $\Theta_D$ [K]	273.073
Longitudinal sound wave velocity, $v_l$ [m/s]	$7.52 \cdot 10^3$
Transverse sound wave velocity, $v_t$ [m/s]	$4.07 \cdot 10^3$
Average speed of sound, $v_m$ [m/s]	$4.54 \cdot 10^3$

Poisson ratio,  $\nu$ , representing the stability of solid against shear deformation, has values between  $-1$  and  $0.5$  for linear and elastic solid. Compound with a large Poisson ratio has good plasticity. As seen in Table 3, the compound under interest has  $\nu = 0.294$  which makes the compound stable and linearly elastic solid. Furthermore,  $\beta'$ -SrTa<sub>2</sub>O<sub>6</sub> crystal is classified as ductile material due to  $\nu > 0.26$  and  $G_v/B_v < 0.57$  [46].

The other fundamental parameters are Debye temperature and sound velocities which are inserted in Table 3. The temperature of the crystal's highest normal mode vibration is called the Debye temperature, which correlates elastic properties with the thermodynamic properties. Most of the compounds have Debye temperature in the range of 200–400 K. The Debye temperature of the compound under investigation is above 400 K. Sound velocity in an anisotropic material is strongly dependent on the propagation direction. The calculated longitudinal, transverse and average sound velocities are listed in Table 3. Therefore,  $\beta'$ -SrTa<sub>2</sub>O<sub>6</sub> crystal is hard with a large wave velocity and has high thermal conductivity.

### 3.5. Dynamical and thermodynamic properties

Studying the vibrational properties and energies of phonons is important for crystal structures because it provides plenty of information about the dynamical properties of the material. The phonon dispersion of the  $\beta'$ -SrTa<sub>2</sub>O<sub>6</sub> crystal under LDA was obtained. The obtained phonon dispersion and phonon density of states (PHDOS) along the principal symmetry direction of the Brillouin zone are given in Fig. 6. Since there are 46 atoms in the unit cell of the  $\beta'$ -SrTa<sub>2</sub>O<sub>6</sub> crystal and 3 degrees of freedom for each atom, there are 138 modes in total. The phonon dispersion confirms the existence of the gap between acoustic branches and optical ones. Furthermore, as it can be seen in Fig. 6, the modes descend into the negative region indicating a dynamically unstable situation for a crystal.

To use a compound in a high-temperature application, it is vital to compute its thermodynamic properties [47]. The Debye temperature ( $\Theta_D(K)$ ), which is related

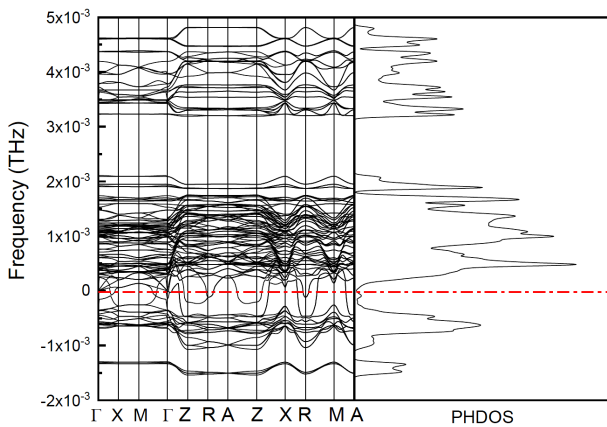


**Figure 6.** Phonon dispersion and phonon density of states for  $\beta'$ -SrTa<sub>2</sub>O<sub>6</sub> crystal as calculated with the ABINIT-LDA code

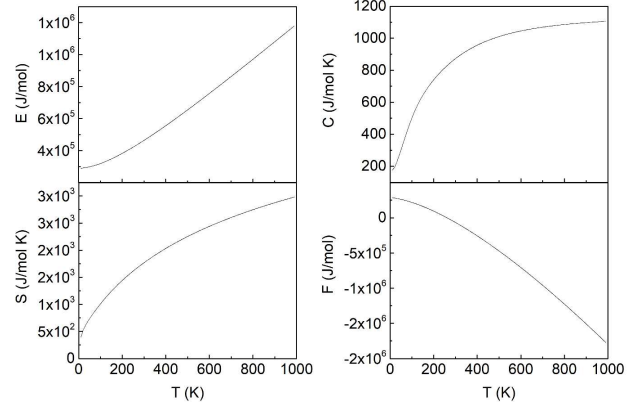


**Figure 7.** The dependences of internal energy ( $E$ ), free energy ( $F$ ), entropy ( $S$ ) and heat capacity ( $C$ ) on temperature for a  $\beta'$ -SrTa<sub>2</sub>O<sub>6</sub> crystal

to the highest frequency modes of vibration, helps researchers to compute thermodynamic properties of the material such as thermal expansion, specific heat, melting temperature, etc. Predicted temperature-dependent constant volume heat capacity,  $C_V$ , is shown in Fig. 7 and one sharp rise is immediately seen in temperature values less than 400 K. At high-temperature values,  $C_V$  converges to a constant value (around  $1100 \text{ J mol}^{-1} \text{ K}^{-1}$ ), the so-called the Dulong-Petit limit.

The zero temperature values  $F_0$  and  $E_0$  do not vanish because of zero-point motion. Figure 7 displays the calculated internal energy ( $E$ ), entropy ( $S$ ), heat capacity ( $C$ ) and Helmholtz free energy ( $F$ ) within the range of temperatures from 0 to 1000 K at zero pressure. It can be seen from Fig. 7 that when the temperature increases, the internal energy increases almost linearly with temperature. The calculated  $S$  increases and  $F$  decreases continually for the compound. There are no literature reports for the experimental values of the thermal properties, so we cannot estimate the errors between our calculated results and experiment. Our results should be considered as predictions and could serve for comparison with further works.

## IV. Conclusions

Theoretical calculation based on the Density Functional Theory is used to calculate structural, electronic, optical, elastic, thermodynamic and thermal properties of  $\beta'$ -SrTa<sub>2</sub>O<sub>6</sub> crystal. The electronic structure calculation shows that the compound is classified as a semiconductor with an indirect band transition. The optical properties were also investigated and showed some interesting results together with their potential applications. The calculated elastic constant reveals that the compound is mechanically stable. Moreover, according to three models, bulk modulus, shear modulus, Young modulus, and Poisson's ratio were calculated and discussed. Constant volume-specific heat capacity figure reveals that heat capacity obeys the  $T^3$  law dependence and becomes nearly constant when the temperature exceeds 400 K. These results may provide theoretical in-

formation for the potential use of the material in technological applications.

## References

1. S.K. Yoon, H.G. Lee, W.S. Lee, E.S. Kim, "Dielectric properties of  $ZnNb_2O_6$ /epoxy composites", *J Electroceramics*, **30** (2013) 93–97.
2. H.-J. Lee, I.-T. Kim, K.S. Hong, "Dielectric properties of  $AB_2O_6$  compounds at microwave frequencies (A = Ca, Mg, Mn, Co, Ni, Zn, and B = Nb, Ta)", *Jpn. J. Appl. Phys.*, **36** (1997) L1318–L1320.
3. C.C. Lee, W.L. Lee, J.-Y. Lin, C.C. Tsuei, J.G. Lin, F.C. Chou, "Superconducting to spin-glass state transformation in  $\beta$ -pyrochlore  $K_xOs_2O_6$ ", *Phys. Rev. B*, **83** (2011) 104503.
4. R. Maruthi, M.S. Seehra, S. Ghosh, R. Medwal, R.S. Rawat, B. Weise, E.S. Choi, S. Thota, "Determination of the tricritical point, H–T phase diagram and exchange interactions in the antiferromagnet  $MnTa_2O_6$ ", *J. Phys. Condens. Matter*, **34** (2022) 155801.
5. U. Duman, M. Aycibin, Ö.F. Özdemir, "The electronic, structural, and optical properties of  $CaNb_2O_6$  compound: Theoretical study", *Phys. Status Solidi B*, **258** (2021) 2100416.
6. T.A. Evans, "Development of antimony-containing catalysts and semiconductors for (photo)electrochemical fuel production", *Ph.D. Thesis*, The University of Wisconsin - Madison, USA, 2020.
7. N. Basavaraju, S.C. Prashantha, B.S. Surendra, T.R. Shashi Shekhar, M.R. Anil Kumar, C.R. Ravikumar, N. Raghavendra, T.S. Shashidhara, "Structural and optical properties of  $MgNb_2O_6$  NPs: Its potential application in photocatalytic and pharmaceutical industries as sensor", *Environ. Nanotechnol., Monit. Manag.*, **16** (2021) 100581.
8. A.B. Christian, A. Rebello, M.G. Smith, J.J. Neumeier "Local and long-range magnetic order of the spin 3/2 system  $CoSb_2O_6$ ", *Phys. Rev. B*, **92** (2015) 174425.
9. D.A. Maltsev, Y.V. Lomachuk, V.M. Shakhova, N.S. Mosyagin, L.V. Skripnikov, A.V. Titov, "Compound-tunable embedding potential method and its application to calcium niobate crystal  $CaNb_2O_6$  with point defects containing tantalum and uranium", *Phys. Rev. B*, **103** (2021) 205105.
10. N.B. Hatırmaz, "Synthesis and dielectric properties of  $ZnNb_2O_6$  microwave dielectric ceramic by sol-gel combustion method", *Ph.D. Thesis*, Marmara University, Turkey, 2010.
11. E. Bayer, R. Gruehn, "Polymorphie von  $SrTa_2O_6$ ", *Zeitschrift Anorg. Allge. Chemie*, **511** (1984) 176–184.
12. V.Y. Kunin, Yu.K. Tarnopol'skii, N.A. Shturbina, "Electrophysical characteristics of strontium tantalate", *Soviet Phys. J.*, **32** (1989) 556–559.
13. J.-K. Lee, H.-J. Jung, O. Auciello, "Electrical characterization of  $Pt/SrBi_2Ta_2O_9/Pt$  capacitors fabricated by the pulsed laser ablated deposition technique", *J. Vac. Sci. Technol. A*, **14** (1996) 900.
14. P.J. Ollivier, T.E. Mallouk, "A "Chimie Douce" synthesis of perovskite-type  $SrTa_2O_6$  and  $SrTa_{2-x}Nb_xO_6$ ", *Chem. Mater.*, **10** (1998) 2585–2587.
15. H. Kato, A. Kudo, "Photocatalytic decomposition of pure water into  $H_2$  and  $O_2$  over  $SrTa_2O_6$  prepared by a flux method", *Chem. Lett.*, **28** (1999) 1207–1208.
16. E. Tokumitsu, G. Fujii, H. Ishiwa, "Nonvolatile ferroelectric-gate field effect transistors using  $SrBi_2Ta_2O_9/Pt/SrTa_2O_6/SiON/Si$  structures", *Appl. Phys. Lett.*, **75** (1999) 575.
17. W.-J. Lee, I.-K. You, S.-O. Ryu, B.-G. Yu, K.-I. Cho, S.-G. Yoon, et al., " $SrTa_2O_6$  thin films deposited by plasma-enhanced atomic layer deposition", *Jpn. J. Appl. Phys.*, **40** (2001) 6941–6944.
18. W. Sakamoto, Y. Horie, T. Yogo, S. Hirano, "Synthesis and properties of highly oriented  $(Sr,Ba)(Nb,Ta)_2O_6$  thin films by chemical solution deposition", *Jpn. J. Appl. Phys.*, **40** (2001) 5599–5604.
19. B.-G. Chae, W.-J. Lee, I.-K. You, S.-O. Ryu, M.-Y. Jung, B.-G. Yu, "New high-k  $SrTa_2O_6$  gate dielectrics prepared by plasma-enhanced atomic layer chemical vapor deposition", *Jpn. J. Appl. Phys.*, **41** (2002) L729–L731.
20. S. Regnery, R. Thomas, P. Ehrhart, "Thin films for high-dielectric applications grown by chemical vapor deposition on different substrates", *J. Appl. Phys.*, **97** (2005) 73521.
21. S. Regnery, R. Thomas, H. Haselier, P. Ehrhart, R. Waser, P. Lehnen, S. Miedl, M. Schumacher, "MOCVD of  $SrTa_2O_6$  thin films for high-k applications", *MRS Proc.*, **811** (2003) 375–380.
22. M. Silniskas, M. Lisker, E. Burte, P. Veit, "Structural and electrical characterization of high-k strontium tantalate deposited by liquid delivery MOCVD", *Integr. Ferroelectr.*, **86** (2006) 31–39.
23. H. Muthurajan, H.H. Kumar, N. Koteswara Rao, S. Pradhan, R.K. Jha, V. Ravi, "Low temperature synthesis of  $SrNb_2O_6$  and  $SrTa_2O_6$  using hydroxide precursor", *Mater. Lett.*, **62** (2008) 892–894.
24. L. Lu, T. Nishida, M. Echizen, K. Uchiyama, Y. Uraoka, "Thickness dependence of electrical properties for high-k  $SrTa_2O_6$  thin films fabricated by sol-gel method", *Jpn. J. Appl. Phys.*, **50** (2011) 03CA05.
25. E. Lee, C.H. Park, D.P. Shoemaker, M. Avdeev, Y. Kim, "Crystal structure analysis of tungsten bronzes  $\beta$ - $SrTa_2O_6$  and  $\beta'$ - $SrTa_2O_6$  by synchrotron X-ray and neutron powder diffraction", *J. Solid State Chem.*, **191** (2012) 232–238.
26. L. Lu, T. Nishida, M. Echizen, K. Uchiyama, Y. Uraoka, "Capacitance-voltage and leakage-current characteristics of sol-gel-derived crystalline and amorphous  $SrTa_2O_6$  thin films", *Thin Solid Films*, **520** (2012) 3620–3623.
27. L. Lu, T. Nishida, M. Masahiro, E. Yasuaki, I. Kiyoshi Uchiyama, Y. Uraoka, "Effects of Si and Ti impurities on electrical properties of sol-gel-derived amorphous  $SrTa_2O_6$  thin films by UV/ $O_3$  treatment", *Appl. Phys. A*, **112** (2013) 425–430.
28. L.L. Noto, M.Y.A. Yagoub, O.M. Ntwaeaborwa, H.C. Swart, "Persistent photoluminescence emission from  $SrTa_2O_6:Pr^{3+}$  phosphor prepared at different temperatures", *Ceram. Int.*, **41** (2015) 8828–8836.
29. Y. Su, Y. Zhao, Y. Zhao, J. Lang, X. Xin, X. Wang, "Novel ternary component  $Ag-SrTa_2O_6/g-C_3N_4$  photocatalyst: Synthesis, optical properties and visible light photocatalytic activity", *Appl. Surf. Sci.*, **358** (2015) 213–222.
30. J.-Y. Kim, Y.-I. Kim, "Local structure and dielectric behavior of tetragonal tungsten bronzes  $\beta$ - $SrTa_2O_6$  and  $\beta'$ - $SrTa_2O_6$ ", *J. Ceram. Soc. Jpn.*, **123** (2015) 419–422.
31. S.P. Adhikari, Z.D. Hood, H. Wang, R. Peng, A. Krall, H. Li, V.W. Chen, K.L. More, Z. Wu, S. Geyer, A. Lachgar, "Enhanced visible light photocatalytic water reduction

- from a  $g\text{-C}_3\text{N}_4/\text{SrTa}_2\text{O}_6$  heterojunction”, *Appl. Catal. B Environ.*, **217** (2017) 448–458.
32. T. Takahashi, T. Hoga, R. Miyanaga, M.N. Fujii, Y. Ishikawa, Y. Uraoka, K. Uchiyama, “SrTa<sub>2</sub>O<sub>6</sub> induced low voltage operation of InGaZnO thin-film transistors”, *Thin Solid Films*, **665** (2018) 173–178.
  33. T. Takahashi, T. Hoga, R. Miyanaga, K. Oikawa, M.N. Fujii, Y. Ishikawa, Y. Uraoka, K. Uchiyama, “Improvement of amorphous InGaZnO thin-film transistor using high-k SrTa<sub>2</sub>O<sub>6</sub> as gate insulator deposited by sputtering method”, *Phys. Status Solidi A*, **216** (2019) 1700773.
  34. P. Blaha, K. Schwarz, F. Tran, R. Laskowski, G.K.H. Madsen, L.D. Marks, “WIEN2k: An APW+lo program for calculating the properties of solids”, *J. Chem. Phys.*, **152** (2020) 74101.
  35. X. Gonze, B. Amadon, G. Antonius, F. Arnardi, L. Baguet, J.M. Beuken, J. Bieder, F. Bottin, J. Bouchet, E. Bousquet, N. Brouwer, F. Bruneval, G. Brunin, T. Cavignac, J.B. Charraud, W. Chen, M. Côté, S. Cottenier, J. Denier, G. Geneste, J.W. Zwanziger, “The ABINIT project: Impact, environment and recent developments”, *Comput. Phys. Commun.*, **248** (2020) 107042.
  36. K. Momma, F. Izumi, “VESTA 3 for three-dimensional visualization of crystal, volumetric and morphology data”, *J. Appl. Crystallogr.*, **44** (2011) 1272–1276.
  37. J.P. Perdew, A. Ruzsinszky, G.I. Csonka, O.A. Vydrov, G.E. Scuseria, L.A. Constantin, X. Zhou, K. Burke, “Restoring the density-gradient expansion for exchange in solids and surfaces”, *Phys. Rev. Lett.*, **100** (2008) 136406.
  38. Y. Zhuo, A. Mansouri Tehrani, J. Brgoch, “Predicting the band gaps of inorganic solids by machine learning”, *J. Phys. Chem. Lett.*, **9** (2018) 1668–1673.
  39. F. Tran, P. Blaha, “Accurate band gaps of semiconductors and insulators with a semilocal exchange-correlation potential”, *Phys. Rev. Lett.*, **102** (2009) 226401.
  40. N. Troullier, J.L. Martins, “Efficient pseudopotentials for plane-wave calculations”, *Phys. Rev. B*, **43** (1991) 1993–2006.
  41. M. Fuchs, M. Scheffler, “Ab initio pseudopotentials for electronic structure calculations of poly-atomic systems using density-functional theory”, *Comput. Phys. Commun.*, **119** (1999) 67–98.
  42. W. Kohn, L.J. Sham, “Self-consistent equations including exchange and correlation effects”, *Phys. Rev.*, **140** (1965) A1133–A1138.
  43. E. Lee, C.-H. Park, D.P. Shoemaker, M. Avdeev, Y.-I. Kim, “Crystal structure analysis of tungsten bronzes  $\beta\text{-SrTa}_2\text{O}_6$  and  $\beta'\text{-SrTa}_2\text{O}_6$  by synchrotron X-ray and neutron powder diffraction”, *J. Solid State Chem.*, **191** (2012) 232–238.
  44. H. Xiao, J. Tahir-Kheli, W.A. Goddard, “Accurate band gaps for semiconductors from density functional theory”, *J. Phys. Chem. Lett.*, **2** (2011) 212–217.
  45. M. Born, K. Huang, M. Lax, “Dynamical theory of crystal lattices”, *Am. J. Phys.*, **23** (1955) 474.
  46. W. Bao, D. Liu, P. Li, Y. Duan, “Structural properties, elastic anisotropies and thermal conductivities of tetragonal LnB<sub>2</sub>C<sub>2</sub> (Ln = Rare Earth) compounds from first-principles calculations”, *Ceram. Int.*, **45** (2019) 1857–1867.
  47. M. Khokon Miah, K. Monower Hossain, M. Atikur Rahman, M. Rasheduzzaman, S.K. Mitro, J. Krishna Modak, Md. Zahid Hasan, “Comprehensive study on the physical properties of tetragonal LaTGe<sub>3</sub> (T = Rh, Ir, or Pd) compounds: An ab initio investigation”, *AIP Adv.*, **11** (2021) 25046.